International Communications in Heat and Mass Transfer 158 (2024) 107926

Contents lists available at ScienceDirect

International Communications in Heat and Mass Transfer

journal homepage: www.elsevier.com/locate/ichmt

3D lattice Boltzmann simulation of vapor chambers with dimensions approaching capillary length

Yuhao Zhu, Yifan Zhang, Zhichun Liu *, Wei Liu

School of Energy and Power Engineering, Huazhong University of Science and Technology (HUST), Wuhan 430074, China

ARTICLE INFO

Keywords:
Vapor chamber
Microstructured surface
Porous structure
Self-propelled droplet transport
LBM

ABSTRACT

When the vapor chamber size is close to the capillary length, the influence of gravity on droplets and bubbles can be negligible and the thermal resistance can also increase significantly due to the reduced wick capillary transport capacity. In this paper, the operation of vapor chambers with dimensions approaching the capillary length is simulated by a three-dimensional multiple-relaxation-time lattice Boltzmann model. Improvements are made to the quartet structure generation set algorithm, enabling the generated porous structures to be fully connected in all directions, rendering it more suitable for the simulation of three-dimensional heat transfer problems. The results indicate that a lower filling ratio can facilitate the bursting of bubbles upon contact with the fluctuating liquid surface, thereby enhancing phase change heat transfer. In addition, by tracking the fluid transport in porous structures and calculating the thermal resistance, it is demonstrated that the increase in porosity can lead to a higher critical heat flux. Additional microstructures can be created on the condensation surface to enhance dropwise nucleation and reflux. The present work provides possible guidelines to optimize the heat transfer performance of vapor chambers with dimensions close to the capillary length.

1. Introduction

With the continuous miniaturization and integration of electronic products, the rapid increase in heat flux brings persistent challenges to the thermal management of electronics [1–3]. The emergence of vapor chamber (VC) provides an efficient passive solution to dissipate highly concentrated heat flux, and it is therefore widely applied in solar collectors [4], portable electronic devices [5] and light-emitting diodes [6]. For portable electronic products, ultra-thin vapor chambers (UTVCs) with an overall thickness of <2 mm are the preferred choice. In order to strengthen the heat transfer performance of UTVCs, researchers have carried out a lot of work on the design of the capillary wick structure [5,7,8], the selection of the working fluids [9], and the vapor-liquid transport mechanism [10]. However, when the thickness is <0.3 mm, the thermal resistance of UTVC will increase dramatically due to the reduced wick capillary transport capacity and the increase of thermal resistance of vapor diffusion and flow resistance [11]. Studies has shown that the capillary limit is one of the main factors that limits the heat transfer performance of VCs, which occurs when the evaporation rate of the working fluid is faster than the replenishment of the liquid through wick structure [12]. Therefore, investigating the influence of different structural parameters on the heat transfer performance of VCs becomes essential. At the same time, strengthening fluid reflux through additional means could be one of the concerns of VC optimization in the future. Recently, it has been proposed that the droplets trapped by microstructures can take off from the superhydrophobic surface by the release of surface energy [13,14]. The spontaneous single-droplet jumping was realized by rationally designing the grooves to limit the growth of droplets with the instantaneous dimensionless jumping velocity ~ 0.95, which is much higher than that of the conventional passive approaches (0.2–0.3) [15]. The calculation showed that the droplet jumping induced by Laplace pressure difference possesses a higher energy conversion efficiency than coalescence-induced droplet jumping. In addition, by designing the microstructures appropriately, it is possible to further control the jumping direction of the liquid droplets [15,16]. The enhancement of droplet jumping velocity manifests that such a self-propelling mode can be potentially applied in the reflux of phase change heat transfer elements.

In terms of numerical simulations, lattice Boltzmann method (LBM) has been widely applied to simulate mesoscopic phase change heat transfer problems [17–19]. Recently, Li et al. [20] proposed a three-dimensional non-orthogonal multiple-relaxation-time (MRT)

* Corresponding author at: School of Energy and Power Engineering, Huazhong University of Science and Technology (HUST), Wuhan 430074, China.
E-mail address: zcliu@hust.edu.cn (Z. Liu).

https://doi.org/10.1016/j.icheatmasstransfer.2024.107926

Available online 10 August 2024

multiphase LB model, which both simplifies the implementation of the method and ensures the numerical accuracy and is considered as an alternative to the conventional orthogonal MRT-LB model. MRT LBM has been employed to study phase change processes, including pool boiling [21,22] and condensation [17,23]. Wu et al. [24] applied a Bhatnagar, Gross, and Krook (BGK) model and studied the effects of surface wettability on the boiling process inside VCs. Furthermore, Ji et al. [25] also applied a 2D MRT LBM in the simulation and analyzed the effects of surface wettability on thermal performance of VCs. The existing LBM simulations are mainly focused on pool boiling. Theoretical analysis indicates that the bubble departure radius is generally on the order of the capillary length, based on the static force balance between surface tension and buoyancy [26]. However, with the miniaturization of the vapor chamber, the thickness of VCs can be close to or even thinner than the capillary length, indicating that bubbles are difficult to detach from the surface under the help of buoyancy. Instead, the bubbles will rupture prematurely during the growth process when they come into contact with the gas-liquid interface. In addition, the effect of gravity on the droplet reflux is also negligible. Therefore, investigating the phase change heat transfer inside VCs with dimensions close to or smaller than the capillary length is of great importance. According to experimental studies [27], the bottom capillary wick that supplies the central heating region is also crucial to prevent VCs from the dry-out under high heat flux, which is often simplified in simulations. Generally, the porous wick can be generated by quartet structure generation set (QSGS) in LBM simulations [28]. The specific algorithm process is as follows: randomly distributing growth nuclei within the given region. Each growth nucleus grows towards the neighboring lattices until the desired porosity is achieved. Li et al. modified the algorithm to get rid of isolated small cavities and tiny solid phase zones [29]. In terms of heat transfer simulation studies, it requires the continuity of the porous structure to ensure the thermal conductivity in the z direction, while current algorithms mainly focus on the capillary pumping process. Therefore, further improvement is necessary to support the simulation of heat transfer problems.

In this paper, a 3D MRT LBM simulation is carried out for the operation of VCs with dimensions close to the capillary length. The quartet structure generation set (QSGS) algorithm is modified to make it more suitable for the simulation of 3D heat transfer problems. The effects of different conditions including wick porosity and filling ratio on the heat transfer performance of VCs are analyzed. In addition, the potential of microstructures in enhancing fluid reflux of VCs is explored. This work provides a possible guideline for the design of VCs to cope with the reduction of the wick capillary transport capacity during miniaturization of electronic products.

2. Numerical method

2.1. 3D non-orthogonal MRT LB model

In this work, a three-dimensional non-orthogonal MRT LB model is applied to simulate the phase transition in VCs [20]. The evolution equation of the density distribution function can be written as:

$$f_i(\mathbf{x}+\mathbf{e}_i\delta_t, t+\delta_t) = f_i(\mathbf{x},t) - \left(\mathbf{M}^{-1}\mathbf{\Lambda}\mathbf{M}\right)_{ij}\left(f_j(\mathbf{x},t) - f_j^{eq}(\mathbf{x},t)\right) + \delta_t \mathbf{F}_i' \quad (1)$$

where $f_i(\mathbf{x},t)$ is the density distribution function, and $f_i^{eq}(\mathbf{x},t)$ represents the corresponding equilibrium density distribution function. $\mathbf{e}_i$ represents the discrete velocity in the i-th direction, the value of which can be referred to Ref. [18]. $(\mathbf{M}^{-1}\mathbf{\Lambda}\mathbf{M})_{ij}$ is the collision operator, where $\mathbf{M}$ is the transformation matrix and $\mathbf{\Lambda}$ is the diagonal collision matrix. $\mathbf{F}_i'$ is the external force term in the velocity space. By matrix transformation, eq. (1) can be further rewritten as

$$f_i(\mathbf{x}+\mathbf{e}_i\delta_t, t+\delta_t) = \mathbf{M}^{-1}[\mathbf{m} - \mathbf{\Lambda}(\mathbf{m}-\mathbf{m}^{eq}) + \delta_t(\mathbf{I}-\mathbf{\Lambda}/2)\mathbf{S}] \quad (2)$$

where $\mathbf{m} = \mathbf{M}\mathbf{f}$, $\mathbf{m}^{eq} = \mathbf{M}\mathbf{f}^{eq}$, and $\mathbf{I}$ is the unit matrix and $\mathbf{S}$ represents the external force term in the moment space. In this work, the non-orthogonal MRT collision operator based on D3Q19 is adopted [30]. The diagonal matrix of the method is expressed as

$$\mathbf{\Lambda} = diag\left(1,1,1,1,s_e,s_\nu,s_\nu,s_\nu,s_\nu,s_\nu,s_q,s_q,s_q,s_q,s_q,s_q,s_\pi,s_\pi,s_\pi\right) \quad (3)$$

whose elements are the inverse of the relaxation time, and s_ν^{-1} is the relaxation time associated with kinematic viscosity. In this work, $s_e = 0.8$, $s_q = s_\pi = 1.0$. By calculating the distribution function in the velocity space, the macroscopic density and momentum in space can then be obtained by.

$$\rho = \sum_i f_i, \rho\mathbf{u} = \sum_i \mathbf{e}_i f_i + \frac{\delta_t}{2}\mathbf{F} \quad (4)$$

where the external force term $\mathbf{F}$ includes the fluid-fluid interaction force $\mathbf{F}_{int}$, the fluid-solid interaction force $\mathbf{F}_s$ and the gravitational force $\mathbf{F}_g$. The form of the fluid-fluid interaction force adopted in this work is given as [31].

$$\mathbf{F}_{int} = -G_0\psi(\mathbf{x})\sum_i G(\mathbf{x}+\mathbf{e}_i\delta_t)\psi(\mathbf{x}+\mathbf{e}_i\delta_t)\mathbf{e}_i \quad (5)$$

where G_0 is the strength of the interaction and $G(\mathbf{x}+\mathbf{e}_i)$ is the weight. In the D3Q19 model, $G_{1-6} = 1/6$ and $G_{7-18} = 1/12$. The interaction potential $\psi(\mathbf{x})$ can be expressed as

$$\psi(\mathbf{x}) = \sqrt{\frac{2\left(p_{EOS} - \rho c_s^2\right)}{G_0 c^2}} \quad (6)$$

where p_{EOS} can be solved by the equation of state. In this paper, the Peng-Robinson equation of state is adopted. c_s is the lattice sound speed and $c = 1$ is the lattice constant. The fluid-solid interaction force $\mathbf{F}_s$ can be written as

$$\mathbf{F}_s = -G_s\psi(\mathbf{x})\sum_i \omega_i s(\mathbf{x}+\mathbf{e}_i\delta_t)\mathbf{e}_i\delta_t \quad (7)$$

where G_s is the fluid-solid interaction strength, which is related to the surface contact. ω_i is the weighting coefficient, and for D3Q19 model, $\omega_i = 1/3$ $(i = 0)$, $\omega_i = 1/18$ $(i = 1–6)$, $\omega_i = 1/36$ $(i = 7–18)$. $s(\mathbf{x})$ is the indicator function, which is equal to 1 for solid and 0 for fluid at the location of $\mathbf{x}$. The gravitational force $\mathbf{F}_g$ can be written as

$$\mathbf{F}_g = \mathbf{g}\cdot(\rho(\mathbf{x}) - \rho_{ave}) \quad (8)$$

where g is the acceleration of gravity and ρ_{ave} is the average density of the computational area.

The energy equation is solved by introducing another temperature distribution function applying the method proposed by Gong et al. [32], and the evolution equation can be written as

$$g_i(\mathbf{x}+\mathbf{e}_i\delta_t, t+\delta_t) = g_i(\mathbf{x},t) - \frac{1}{\tau_T}\left(g_i(\mathbf{x},t) - g_i^{eq}(\mathbf{x},t)\right) + \delta_t\omega_i\phi \quad (9)$$

where $g_i(\mathbf{x}, t)$ is the temperature distribution function at moment t and position $\mathbf{x}$, $g_i^{eq}(\mathbf{x}, t)$ is the corresponding equilibrium density distribution function. τ_T is the temperature relaxation time. ϕ is the source term associated with the phase change and can be written as [33].

$$\phi = T\left[1 - \frac{1}{\rho c_v}\left(\frac{\partial p}{\partial T}\right)_\rho\right]\nabla\cdot\mathbf{U} + \left[\frac{1}{\rho c_v}\nabla\cdot(\lambda\nabla T) - \nabla\cdot\left(\frac{\lambda}{\rho c_v}\nabla T\right)\right] \quad (10)$$

where $(\partial p/\partial T)_\rho$ can be obtained from the equation of state and $\mathbf{U}$ is the real fluid velocity. Then, the temperature can be obtained by calculating the temperature distribution function

$$T = \sum_i g_i \quad (11)$$

In addition, the physical properties of vapor-liquid interface (e.g., kinematic viscosity, specific heat and thermal diffusivity) can be obtained by the following equation:

$$\chi = \chi_{\text{liquid}} \cdot \frac{\rho - \rho_{\text{vapor}}}{\rho_{\text{liquid}} - \rho_{\text{vapor}}} + \chi_{\text{vapor}} \cdot \frac{\rho_{\text{liquid}} - \rho}{\rho_{\text{liquid}} - \rho_{\text{vapor}}} \tag{12}$$

2.2. Model validation

In order to validate the 3D MRT LB model, the D^2 law is first tested by recording the decrease in the square of droplet diameter during evaporation. Secondly, the change of the condensation droplet radius with time is verified in accordance with the power law, and the grid independence is examined at the same time.

2.2.1. Verification of phase change process

According to D^2 law, the square of the diameter of the droplet should decrease linearly with time. The calculation domain is set to 100 × 100 × 100 l.u. (l.u. denotes the lattice units), and the periodic boundary conditions are set all around. The droplet is placed in the middle of the domain with the radius $r = 30$ l.u. The initial temperature of the saturated droplet is set to $0.85T_c$. The droplet evaporation at different boundary temperatures is calculated by adjusting the difference between the initial boundary temperature and the droplet temperature ΔT. The temperature of the superheated vapor is initialized the same as the boundary temperature. As shown in Fig. 1, the square of droplet diameter decreases linearly with time in three cases with different temperature differences, which is in consistent with D^2 law.

2.2.2. Grid independence verification

Since the study is mainly focused on the simulation of boiling and condensation inside VCs, the droplet condensation process in the closed system is chosen for the grid independence verification. For a 3D single-droplet condensation process, the relationship between the droplet radius and time should satisfy the power law ($R \sim t^a$), whose power law exponent a = 1/3 [34]. As shown in Fig. 2(a), a cold source is set at the center of bottom ($T_{bot} = 0.65T_c$), and the temperature of the top wall is fixed the same as the initial saturation temperature ($T_{top} = T_s = 0.85T_c$). A layer of saturated liquid water is set at the top of the domain during initialization, and the rest of the space is filled with saturated vapor. The simulation results for calculation domain of $L_x \times L_y \times L_z = 60 \times 60 \times 60$ l.u., 90 × 90 × 90 l.u., 120 × 120 × 120 l.u. and 150 × 150 × 150 l.u. are shown in Fig. 2(b). It can be seen that the difference between the simulated exponents and theoretical values is within the acceptable range ($0.23 \leq a \leq 0.5$) [34,35]. Besides, when the computational domain is >120 × 120 × 120 l.u., domain size has no significant influence on the growth of single droplet. Therefore, 120 × 120 × 120 l.u. is chosen for the subsequent simulations.

3. Results and discussion

3.1. Modified porous structure generation algorithm

The generation of porous structures is usually completed by the quartet structure generation set (QSGS) [29,36]. In order to guarantee the accuracy of simulation when calculating three-dimensional thermal conductivity problems, a modified QSGS algorithm is developed in this work, to make sure that the generated structures are completely connected in all directions. Based on the original QSGS, the improved algorithm can further find the discontinuous solid phase parts and make them grow separately. By setting an acceptable porosity deviation range, the generated porous structure can be guaranteed to meet the porosity requirements. The porous generation steps of the modified algorithm are as follows (Fig. 3):

(a) Randomly distribute growth cores as ancestral cores in the space according to the given distribution probability η_d, and number the different ancestral cores (part number $p_{\text{num}} = 1, 2, 3, \ldots, p_{\max}$).
(b) According to the growth probability η_g, each ancestral core extends to the neighboring lattices, and the solid phase lattices grown from the same ancestral core are labeled with the same part number as the ancestor.
(c) Take all solid phase lattices as the growth core, repeat step (2) and count the number of solid phase lattices until the setting porosity η_{sp} is reached.
(d) Find the flow dead zones in the generated porous media domain and convert them to solid phases. Again, find the cores that are not extended and convert them into fluid phases.

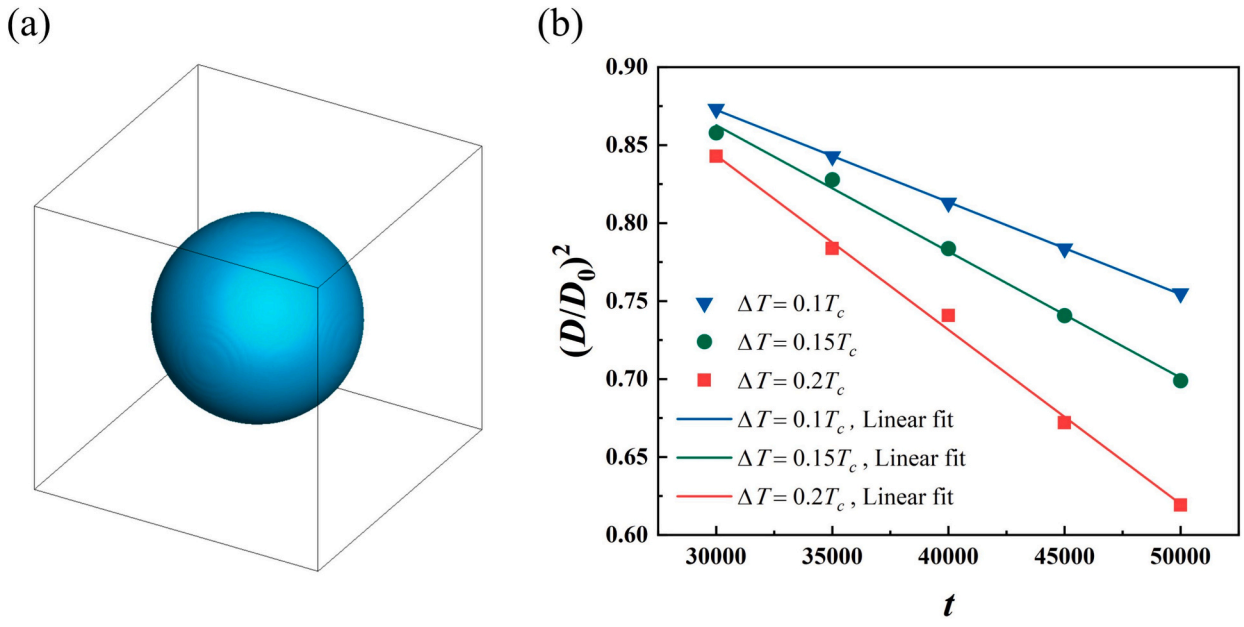

Fig. 1. Evaporation process verification. (a) Schematic diagram of the simulation. (b) Variation of the square of the droplet diameter with time at different boundary temperatures.

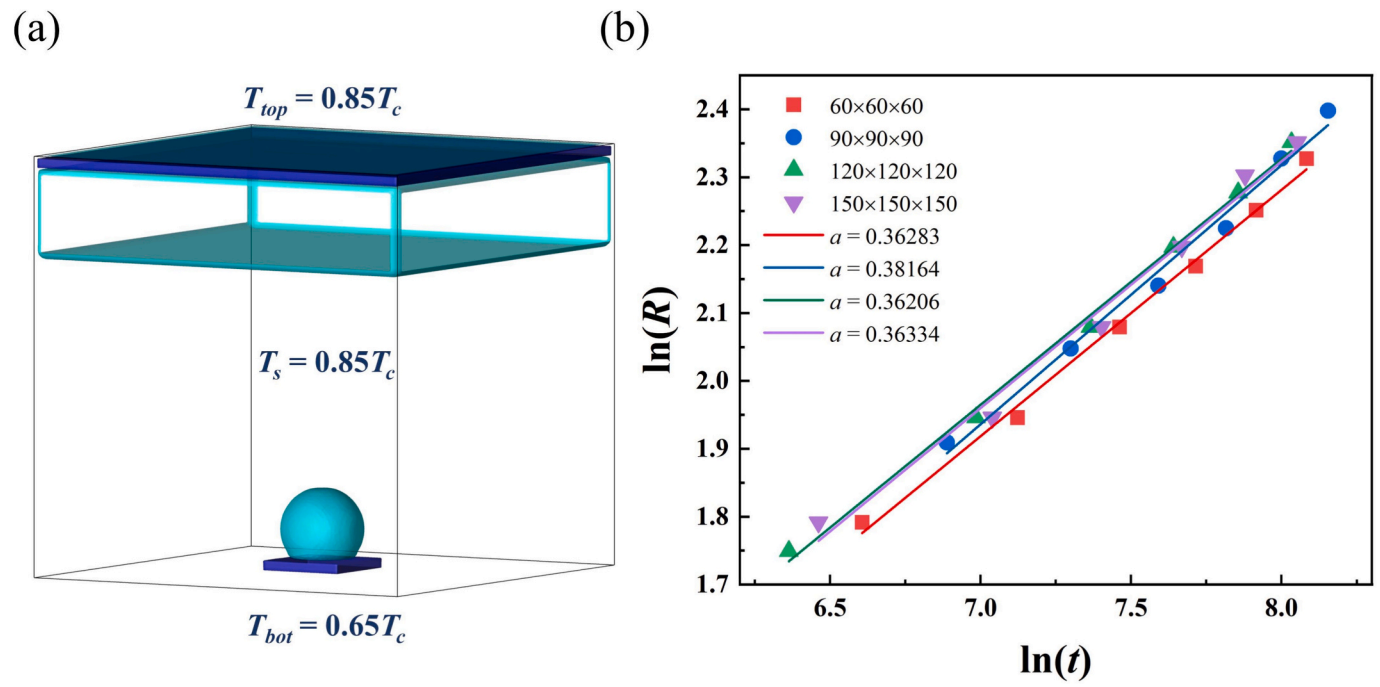

Fig. 2. Grid independence verification. (a) Schematic diagram of condensation. (b) Variation of ln(R) with ln(t) at different lattice resolutions.

(e) Merge the connected parts: traverse the porous media, find the connected solid phase parts, modify their part numbers to the minimum value among them, and obtain a new set of part numbers. For example, the solid $p_{num} = 5$ is connected to the solid part $p_{num} = 1$ in Fig. 3(a). Therefore, assign the label 1 to the solid $p_{num} = 5$, making them a unified whole with $p_{num} = 1$.

(f) Make the isolated parts continue to grow in descending order of number, until they are connected to solid phase parts with smaller part numbers. Then, modify their part numbers to the smaller one. In the end, all the part numbers are reduced to the same value and the generation of porous structures is completed.

(g) Recalculate the porosity, check whether the generated porosity η_{gp} is within the acceptable porosity deviation range $\Delta\eta$, if not, go back to step (2) and regenerate the porous structure.

As shown in Fig. 4(a), the continuity of the structure generated by the original algorithm is analyzed when the setting porosity $\eta_{sp} = 0.2$–0.8. The porous structure is repeatedly grown 30 times and the mean and standard deviation of the number of isolated parts are calculated each time. The results show that the number of isolated parts in the porous structure generated by the original algorithm increases with the increase of porosity. There are no isolated parts observed when the setting porosity η_{sp} is reduced to 0.2. Then the computational efficiency of the improved algorithm is analyzed. When $\Delta\eta = \pm 0.03$, the qualification ratios for different η_{sp} are shown in Fig. 4(a), which represents the proportion of porous structures whose $\eta_{gp} \in (\eta_{sp}\text{-}\Delta\eta, \eta_{sp} + \Delta\eta)$. For the cases $\eta_{sp} = 0.2$–0.5, the qualification ratio is close to 100%, that is, the desired porous structure can be obtained with fewer code cycles. Specifically, a total of 30 times porosity generation results for $\eta_{sp} = 0.5$–0.8 are shown in Fig. 4(b). With the increase of η_{sp}, the resulting continuous structure is more difficult to meet the porosity requirements, indicating that longer computation time is required to obtain the desired porosity.

3.2. Calculation domain and parameter settings

The diagram of the calculation domain is shown in Fig. 5. Constant heat flux boundary condition is adopted at the bottom, with a heating area of 30 × 30 l.u. in the center, and the remaining area is kept adiabatic [37]. The thickness of the bottom solid is 5 l.u. The thickness of the porous structure is 10 l.u., of which the porosity is set as 65%. The constant temperature boundary condition is adopted at the top with $T_{top} = 0.65T_c$. In order to analyze the phenomenon of droplet detachment caused by different mechanisms on the condensing surface, including coalescence-induced jumping and single droplet jumping, the contact angle of the top wall is set to $\theta_{top} = 160°$ [38]. Additional square micropillars are set to enhance condensation nucleation and reflux, with a width of 6 l.u. and a height of 24 l.u. Periodic boundary condition is used for the rest of the periphery. Besides, the halfway bounce-back scheme is adopted for the solid surface, and conjugate boundary condition is applied for the fluid-solid interface. The computational domain is filled with saturated vapor at $0.85T_c$ and a layer of saturated liquid water is initialized at the bottom.

In addition, the capillary length is often used as the characteristic length to correspond the lattice unit to the actual unit [17], which can be written as

$$l_0 = \sqrt{\frac{\sigma}{g(\rho_l - \rho_v)}} \tag{13}$$

where l_0 is the capillary length, g is the gravitational acceleration, ρ_l and ρ_v are the densities of saturated liquid and saturated vapor. In this work, the gravitational acceleration is taken as $g = 3 \times 10^{-5}$ in lattice unit, and the working medium is chosen as water. With the characteristic time chosen as $t_0 = \sqrt{l_0/g}$, the dimensionless time can further be expressed as

$$t^* = \frac{t}{t_0} = gt\sqrt{\frac{\rho_l - \rho_v}{\sigma}} \tag{14}$$

where t is the lattice time. In this study, the capillary length $l_0^{lu} = 81.4$ l.u., the size of the calculation domain $L_x = L_y = L_z \approx 1.5\ l_0$ and the characteristic time $t_0 = 805.3$. To correspond lattice units and real units, the capillary length in real unit is also calculated. In this study, the saturated vapor is set as $0.85T_c$, with coexistence densities, surface tension and gravitational acceleration in real unit $\rho_l = 735.96$ kg/m^3, $\rho_v = 37.77$ kg/m^3, $\sigma = 0.017163$ N/m and $g = 9.81$ m/s^2. Therefore, the calculation result for capillary length in real unit is $l_0^{real} = 1.58$ mm.

The dimensionless heat flux can be calculated by $q^* = q/q_0$, where

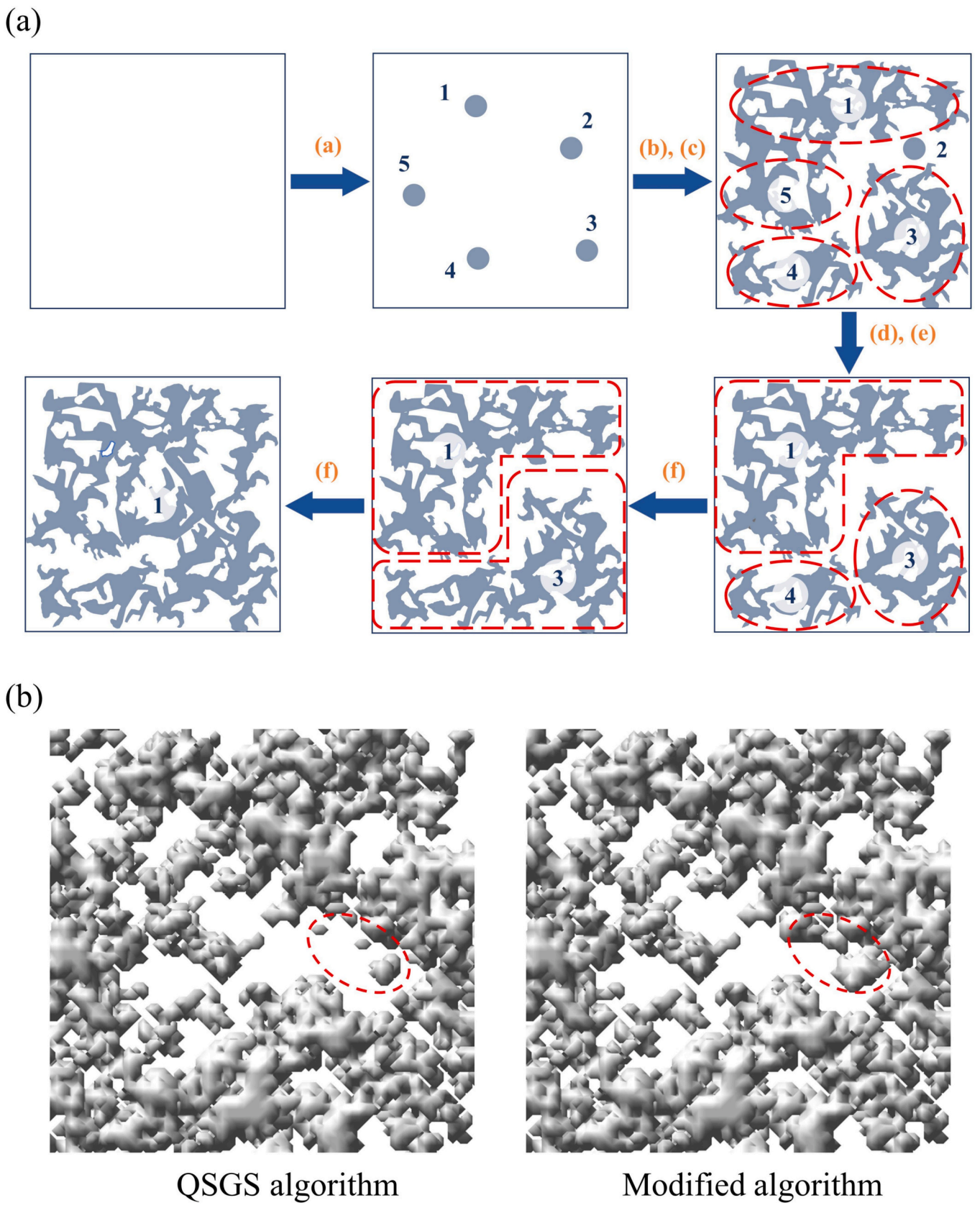

Fig. 3. The generation of porous structures. (a) Flow diagram of the generation of porous structures by modified algorithm. (b) Comparison of the porous structures generated by the original QSGS algorithm and modified algorithm. The size of the computational domain is 60 × 60 × 6 l.u.

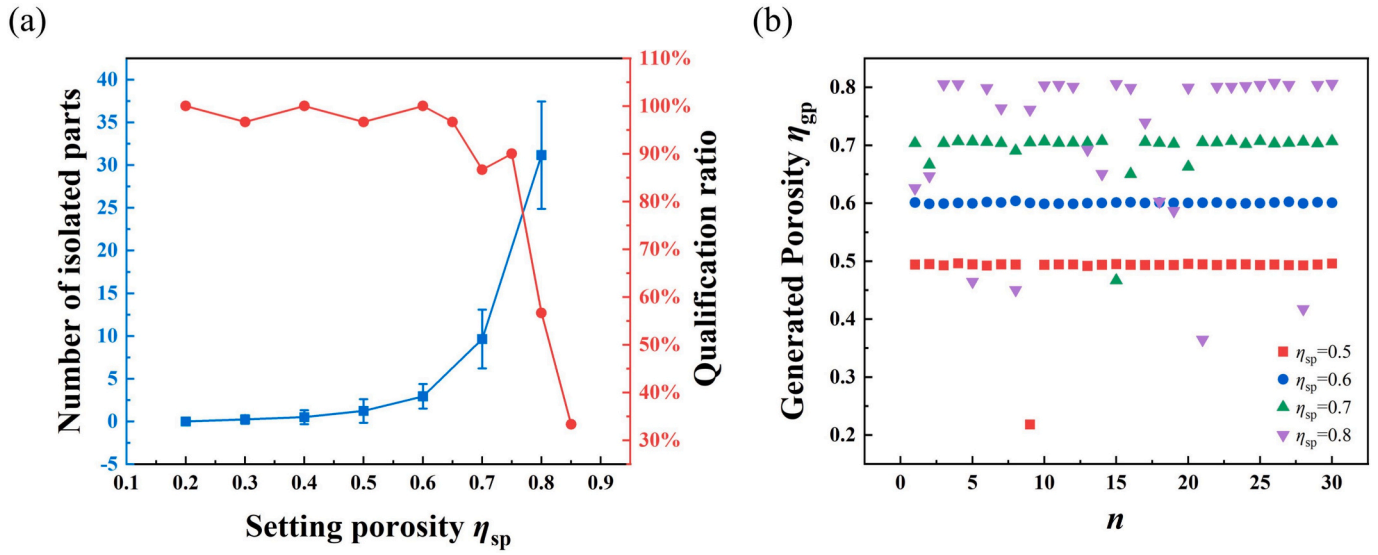

Fig. 4. Quantitative analysis of the modified algorithm. The qualification ratio represents the proportion of porous structures whose $\eta_{gp} \in (\eta_{sp}\text{-}\Delta\eta, \eta_{sp} + \Delta\eta)$. (a) The qualification ratio of the generated porous structure. (b) A total of 30 times porosity generation results for η_{sp} = 0.5–0.8.

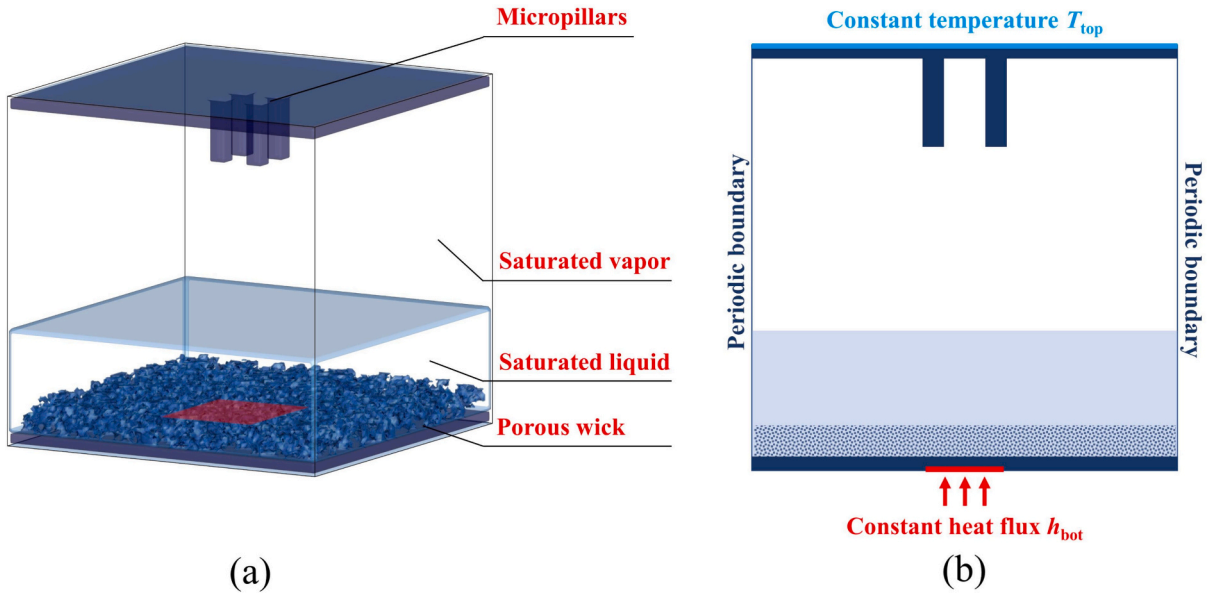

Fig. 5. Schematic diagram of the vapor chamber.

the reference heat flux is defined as [39].

$$q_0 = \frac{\mu_l h_{fg}}{l_0} \tag{15}$$

where μ_l = 0.40 is the liquid dynamic viscosity and h_{fg} = 0.39 is the latent heat which can be obtained by the latent heat calculation method [40]. It should be noted that unless otherwise stated, all variables in this study are expressed in lattice units.

3.3. Phase change phenomena during the operation of VCs

To simulate the operation of the system and observe as many phase change phenomena as possible, four square micropillars are arranged on the condensation surface as a structural unit. The phase change process inside the VC is shown in Fig. 6, with the constant heat flux q = 0.03 (corresponding to q^* = 15.65) and filling ratio α = 35%. It should be noted that the filling ratio in this study is defined as working fluid volume compared to hollow space inside vapor chamber. Following the start-up of the VC, bubbles are first generated in the middle of the capillary wick. As the lateral transfer of heat, small bubbles begin to appear throughout the bottom under the existence of lateral heat conduction. During the heating process, the bubbles do not detach but continue to grow on the surface of the porous structure until they rupture upon contact with the liquid-gas interface. On the other side, the micropillar structure provides nucleation sites for condensation and accelerates the formation of condensate droplets. As presented in Fig. 6, both overflow-induced single-droplet jumping and coalescence-induced droplet jumping are observed during dropwise condensation.

Fig. 7(a) shows the variation of the average heating surface temperature T_{avg} with time under the condition of interval heat flux. And the corresponding bubble dynamics during the heating cessation stage are presented in Fig. 7(c). As the liquid fluctuates, large bubbles break after touching the liquid-vapor interface, while smaller bubbles shrink and disappear with time. The comparison of the temperature variation with

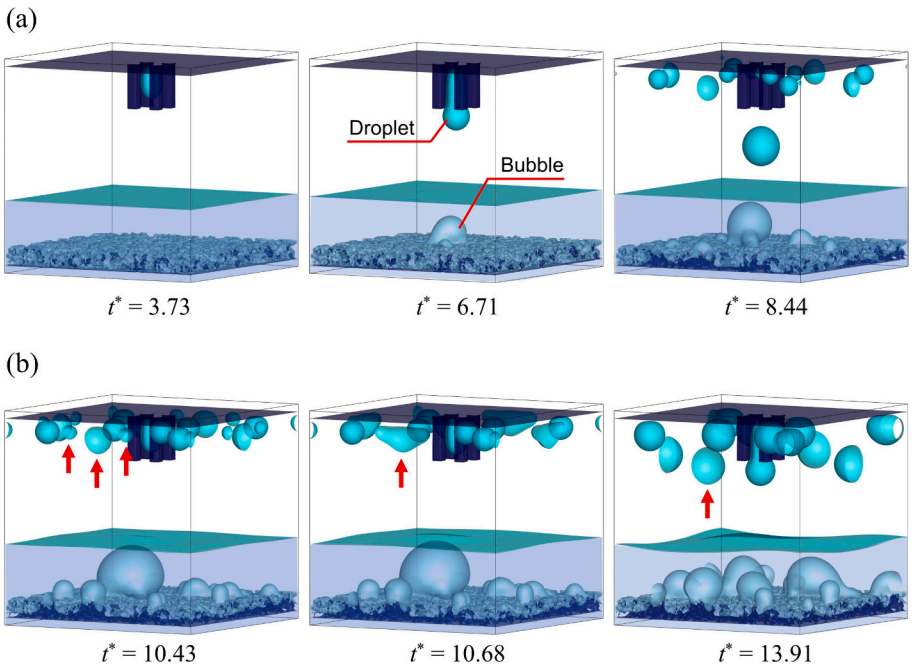

Fig. 6. Operation process of the vapor chamber with $q = 0.03$ and filling ratio $\alpha = 35\%$. (a) Overflow-induced single-droplet jumping. (b) Coalescence-induced droplet jumping.

constant heat flux and interval heat flux is shown in Fig. 7(b). For constant heat flux, the temperature of the heating surface tends to stabilize after $t^* = 15$. Due to the generation and departure of bubbles, the surface temperature still fluctuates slightly after the stable operation of the VC. For interval heat flux, the temperature curve at each heating stage is basically consistent with that of the constant heat flux. After the heating is stopped, the temperature of the heating surface decreases rapidly.

3.4. The influence of porous structures

In this section, effects of porous structures on thermal resistance and the performance of phase change inside the VCs are studied. To visually demonstrate the flow of the working fluid in the porous structure, the velocity vector plot at $t^* = 7.45$ and z = 8 of continuous heating in section 3.3 is selected and presented in Fig. 8(a). During the bubble nucleation and growth process, the working fluid is replenished to the liquid deficient area through the porous wick. In addition to the observable bubbles corresponding to Fig. 8(b), the convergence direction of the velocity vectors can also be used to predict the subsequent bubble nucleation locations in advance.

Fig. 9(a) compares the thermal resistance of VCs with different porosity conditions. The VC thermal resistance can be calculated by

$$R = \frac{T_{\mathrm{avg}} - T_{top}}{q} \tag{16}$$

where T_{avg} is the average heating surface temperature, T_{top} is the condensation surface temperature and q is the constant heat flux. The thermal resistance under four different porosity conditions is calculated for heat flux of 0.1, 0.2, 0.3, and 0.4. The results show that the thermal resistance decreases with the increase of the heat flux which is consistent with the experimental studies [27]. However, for the case of $\eta_p = 50\%$, the heating surface experiences dry-out when the heat flux density exceeds 0.3. Similarly, for the case of $\eta_p = 35\%$, the dry-out occurs when the heat flux density exceeds 0.2. The reason is that the porous wick at the bottom mainly provides lateral capillary force during the heat transfer process to replenish the liquid to the heating area. The resistance of fluid flow in the porous wick is related to permeability: the smaller the permeability, the greater the resistance to fluid flow in the wick. The relationship between permeability and porosity can be expressed by the Carman-Kozeny equation [41].

$$k = \frac{d^2 \eta_{\mathrm{p}}^3}{c\left(1 - \eta_{\mathrm{p}}\right)^2} \tag{17}$$

where k is the permeability, d is the mean pore diameter, and c is a constant. Therefore, the decrease of porosity leads to the increase of flow resistance. In the case of high heat flux, the inability to replenish the working fluid to the heating surface in time can lead to the occurrence of dry-out phenomenon, which means that the critical heat flux decreases as the porosity decreases.

On the other hand, as shown in Fig. 9(a), an increase in porosity under the same heat flux leads to a slight increase in thermal resistance. The main reason is that with the increase of heat flux, bubble disturbance plays an increasingly important role in enhancing heat transfer. A higher lateral liquid replenishment capability of the porous wick makes it more difficult for large bubbles to grow on the surface, resulting in the inability to enhance liquid disturbance through frequent bubble bursting to further enhance the heat transfer efficiency of VCs (Fig. 9(b)). Of course, it should be noted that the failure of large bubbles to burst in time can also lead to the occurrence of partial dry-out. The higher permeability ensures that the VCs can withstand a higher heat flux. Therefore, the selection of porosity should be based on the actual heat transfer requirements. If the heat flux requirements are already met, a smaller porosity can be chosen to provide lower thermal resistance. Otherwise, selecting a porous wick with a higher porosity can ensure a higher critical heat flux.

3.5. The influence of filling ratio

To analyze the effect of different filling ratios on heat transfer performance of the VCs, we selected two typical heat flux densities (q = 0.01 and 0.03) and analyzed the variation of the average temperature on the heating surface ($z = 0$) over time. Additionally, a region on the upper surface of the porous wick ($z = 15$) with the same size as the heating surface is also selected to calculate the average temperature, which is

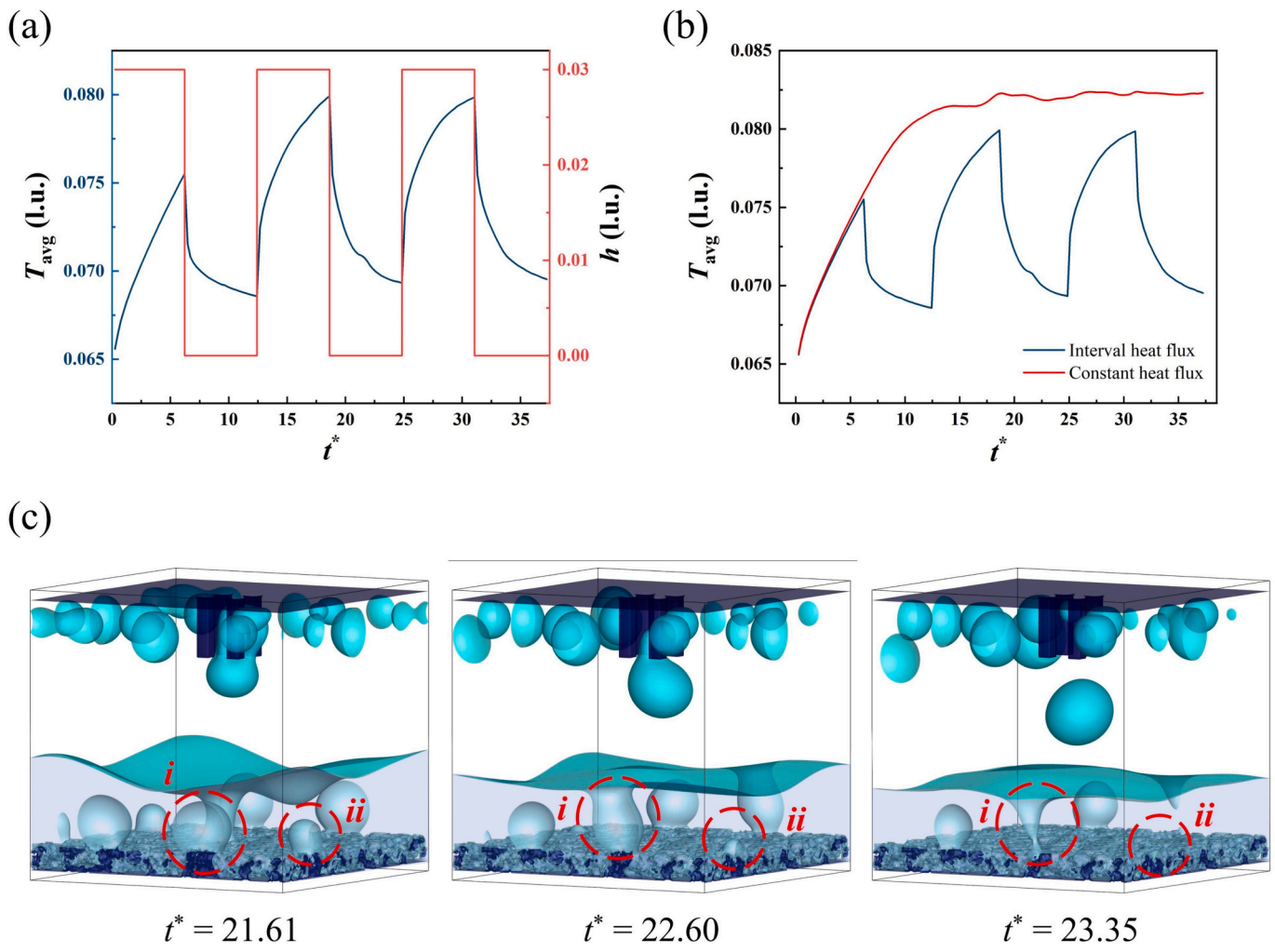

Fig. 7. Operation process of the vapor chamber with interval heat flux. (a) Variation of T_{avg} with time under the condition of interval heat flux. (b) Comparison of temperature variation under constant heat flux and interval heat flux. (c) Dynamic evolution of bubbles during the heating cessation stage.

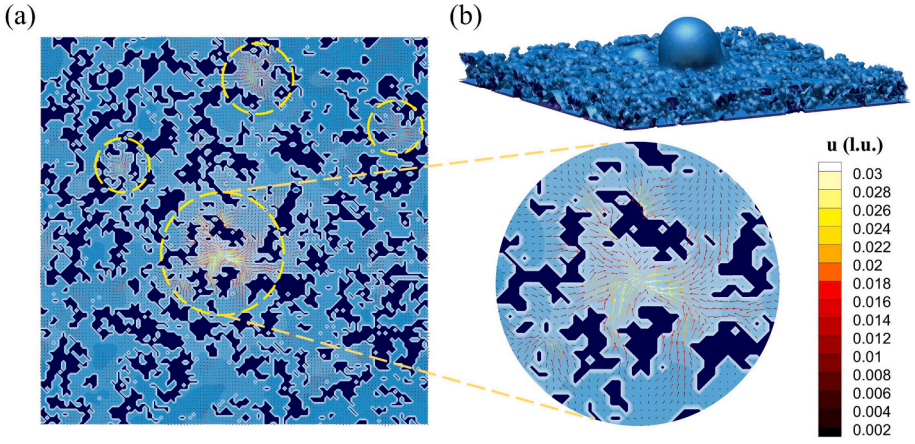

Fig. 8. Transport of working medium in porous wick. (a) Cross section at $z = 8$. (b) Corresponding bottom bubble growth diagram.

intended to reflect the disturbance of bubbles to the liquid. At the same time, the micro-pillar structure on the top is removed to prevent its potential influence under high filling ratios.

As presented in Fig. 10(a), when the heat flux $q = 0.01$, the temperature of the heating surface rises with the increase in the filling ratio. The main reason is that at low heat flux, the thickening of the liquid film leads to an increase in the conduction heat resistance. As a result, the thermal resistance increases with the increase of liquid film thickness. On the other hand, the upper surface of the porous wick exhibits minimal fluctuations in average temperature due to the growth of bubbles. When the heat flux $q = 0.03$ (Fig. 10(b)), the fluctuation in the temperature curve of the upper surface of the porous wick is significantly

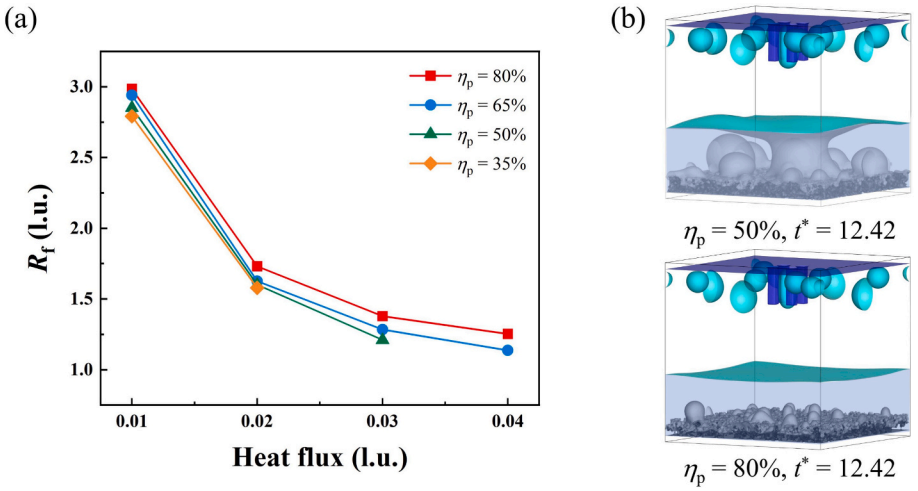

Fig. 9. The influence of porous structures on the operation of VCs. (a) Variation of thermal resistance with heat flux under different porosity conditions. (b) Bubbles on surfaces with different porosity.

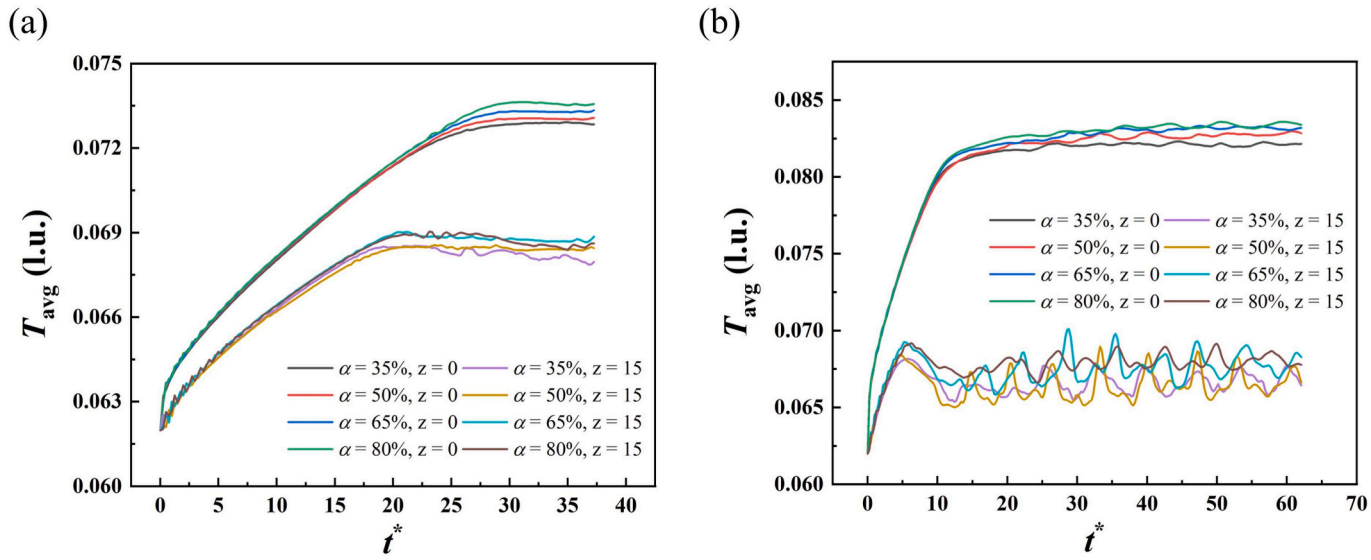

Fig. 10. The effect of filling ratios on the operation of VCs. (a) The temperature variation curve with heat flux $q = 0.01$. (b) The temperature variation curve with heat flux $q = 0.03$.

enhanced, indicating a pronounced intensification of the disturbance caused by bubbles inside the liquid. At the same time, the average temperature of the heating surface is still lower when the filling ratio $\alpha = 35\%$ compared to other conditions. The main reason is that the size of the VCs is chosen to be close to the capillary length, which restricts the bubbles from detaching from the surface of the porous wick under the effect of buoyancy. Bubbles can only rupture through contacting with the gas-liquid contact surface. The higher the filling ratio, the larger the bubbles need to grow to reach the gas-liquid interface, thereby inhibiting phase change heat transfer. When the filling ratio is lower, bubbles are more likely to burst after contacting the fluctuating liquid surface during the growth process, thereby enhancing phase change heat transfer. Therefore, in the case of ensuring that partial dry-out does not occur, for a VC with a size close to or smaller than the capillary length, choosing a lower filling ratio will result in a lower thermal resistance.

3.6. The influence of microstructures on condensation surfaces

The effect of the number of structural units on the variation of heating area is studied subsequently. Fig. 11(a) compares the thermal resistance of VCs for smooth condensation surface and microstructured surface at different heat fluxes when the filling ratio $\alpha = 35\%$. Structure X represents a structure with X structural units. The results show that the impact of different condensation surfaces on thermal resistance is relatively minor. The main reason is that the filling ratio is sufficient to prevent VCs from partial dry-out, and therefore the reflux effect of the microstructure is not obvious. When the filling ratio is further reduced to 20% (Fig. 11(b)), the fluctuation of the average temperature over time with different condensation surfaces becomes evident due to the appearance of partial dry-out, and the enhancement of microstructure on reflux begins to manifest. The specific configurations of the three structures can be referred to Fig. 11(c). The average heating surface temperature of the VC with micropillars remains consistently lower than that of the VC with smooth condensation surface during the temperature fluctuation. To visualize the enhancement of microstructures on reflux, the evolution of condensation and droplet detachment is presented in Fig. 11(c), with the constant heat flux $q = 0.03$ and filling ratio $\alpha = 20\%$. It is shown that the presence of microstructures greatly accelerates the rate of nucleation. In addition, the micropillars set in the middle also increase the probability of droplets falling to the central heating area.

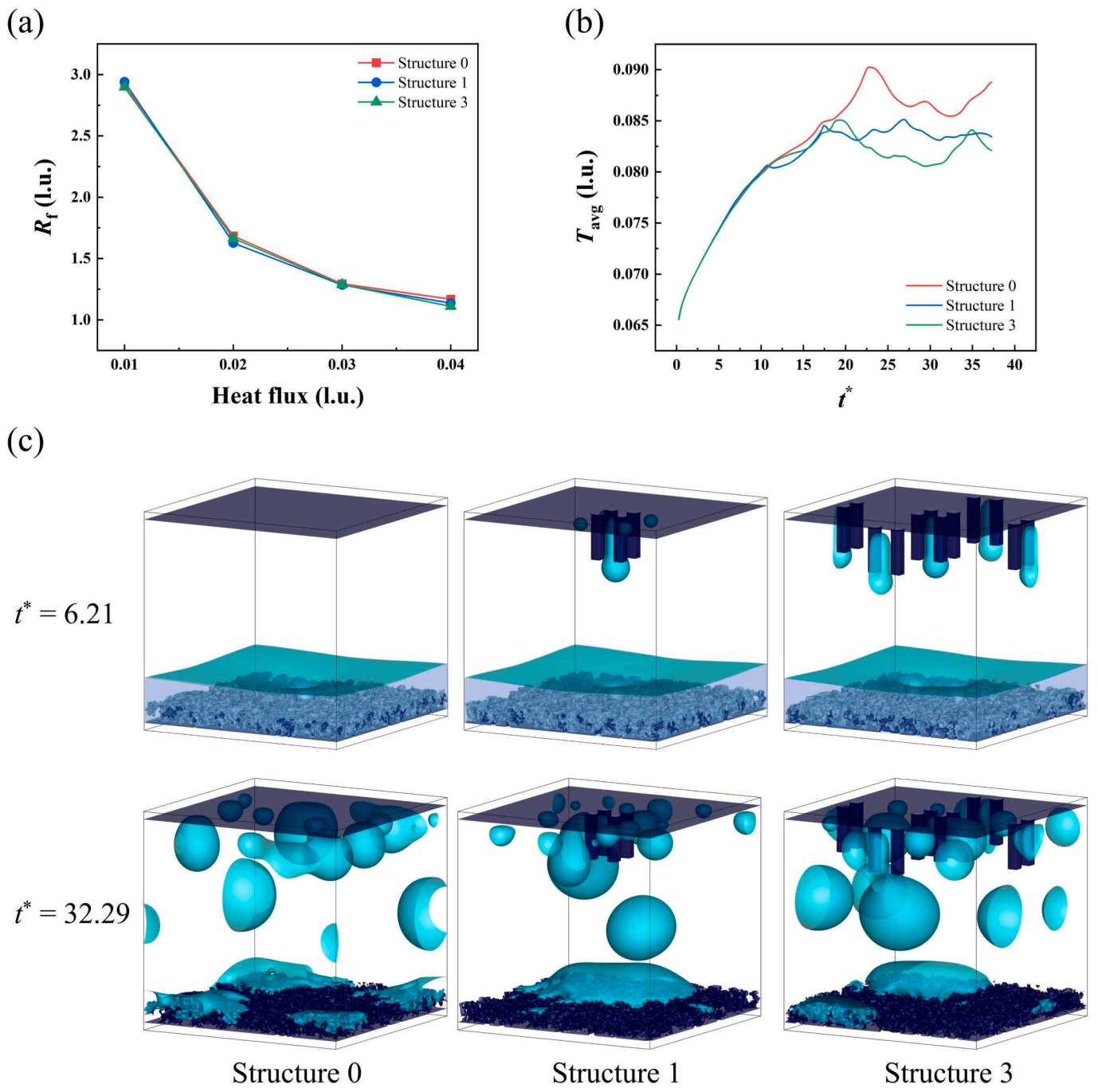

Fig. 11. Comparison of VCs with different structures on condensation surfaces. (a) Variation of thermal resistance with heat flux. (b) Variation of T_{avg} with time. (c) Reflux conditions of different condensation surface structures when the filling ratio is 20%.

Regarding Structure 3, although the increased number of micropillars provides more nucleation sites and enhances the fluid reflux, the probability of droplet deposition in the central heating zone does not increase significantly. In conclusion, for VCs that are prone to local dry-out during the start-up phase, additional microstructures can be fabricated on the condensation surface to enhance nucleation during the initial phase. Besides, the direction of the micropillars can be aligned with the heating surface, which makes it easier for the reflux droplets to cool the heating surface directly.

4. Conclusion

In this paper, a 3D non-orthogonal MRT lattice Boltzmann model is employed to simulate the operation of VCs with dimensions close to the capillary length. The QSGS algorithm is modified for the simulation of heat transfer problems. The effects of wick porosity and filling ratio on the heat transfer performance of VCs are analyzed. Moreover, the potential of microstructures in enhancing fluid reflux of VCs is explored. The main conclusions are summarized as follows:

(1) When the size of the VC is close to the capillary length, the bursting of bubbles is mainly achieved through their contact with the liquid-vapor interface during the growth process. The detachment of droplets from the condensation surface is caused by the release of surface energy, including coalescence-induced

droplet jumping and pinning/stretch-induced single droplet jumping.

(2) The increase in porosity can lead to a decrease in flow resistance, which allows the porous wick to withstand a higher critical heat flux. On the other hand, a higher lateral liquid replenishment capability also makes it more difficult for bubbles to grow, resulting in the inability to enhance liquid disturbance through frequent bubble bursting to further enhance the heat transfer efficiency. Therefore, if the heat flux requirements are already met, a smaller porosity can be chosen to achieve a lower thermal resistance. Otherwise, a porous wick with a higher porosity can ensure a higher critical heat flux.

(3) When ensuring that partial dry-out does not occur, for a VC with dimensions close to the capillary length, choosing a lower filling ratio can result in a lower thermal resistance. The main reason is that the surface tension has a much greater effect than buoyancy, making it difficult for the bubbles to detach under the influence of buoyancy. The higher the filling ratio, the more difficult it is for bubbles to contact the fluctuating liquid-vapor interface and burst.

(4) For VCs that are prone to experiencing local dry-out during the start-up phase, it is possible to create additional microstructures on the condensation surface to enhance dropwise nucleation and reflux during the initial stage. In addition, the direction of the micropillars can be aligned with the heating surface, which makes it easier for the reflux droplets to cool the heating surface directly.

CRediT authorship contribution statement

Yuhao Zhu: Writing – original draft, Validation, Software, Investigation, Conceptualization. **Yifan Zhang:** Writing – review & editing, Investigation. **Zhichun Liu:** Writing – review & editing, Supervision, Funding acquisition. **Wei Liu:** Supervision, Investigation.

Declaration of competing interest

The authors declare that they have no known competing financial interests or personal relationships that could have appeared to influence the work reported in this paper.

Data availability

Data will be made available on request.

Acknowledgments

This work was supported by the National Natural Science Foundation of China (No. 52076088).

References

[1] X. Cheng, G. Yang, J. Wu, Recent advances in the optimization of evaporator wicks of vapor chambers: from mechanism to fabrication technologies, Appl. Therm. Eng. 188 (2021) 116611.
[2] H.C. Cui, W.H. Fan, J. Wang, M.J. Yu, Z.K. Zhang, Z.C. Liu, W. Liu, Characteristics analysis and structure optimization of a hybrid micro-jet impingement/micro-channel heat sink, Appl. Therm. Eng. 245 (2024) 122769.
[3] F. Zhou, J. Zhou, X. Huai, Advancements and challenges in ultra-thin vapor chambers for high-efficiency electronic thermal management: a comprehensive review, Int. J. Heat Mass Transf. 214 (2023) 124453.
[4] G. Chen, Y. Tang, L. Duan, H. Tang, G. Zhong, Z. Wan, S. Zhang, T. Fu, Thermal performance enhancement of micro-grooved aluminum flat plate heat pipes applied in solar collectors, Renew. Energy 146 (2020) 2234–2242.
[5] C. Yan, H. Li, Y. Tang, X. Ding, X. Yuan, Y. Liang, S. Zhang, A novel ultra-thin vapor chamber with composite wick for portable electronics cooling, Appl. Therm. Eng. 226 (2023) 120340.
[6] L. Chen, D. Deng, Q. Huang, X. Xu, Y. Xie, Development and thermal performance of a vapor chamber with multi-artery reentrant microchannels for high-power LED, Appl. Therm. Eng. 166 (2020) 114686.
[7] X. Meng, S. Tan, Z. Yuan, Y. Zhang, L. Chen, Experimental study on the heat transfer performance of a vapour chamber with porous wick structures printed via metallic additive manufacturing, Int. Commun. Heat Mass Transf. 140 (2023) 106496.
[8] L. Duan, Z. Wang, G. Chen, Y. Tang, Y. Sun, G. Zhong, X. Xi, Y. Xu, Capillary wicking in double-scale composite microgroove wicks for copper-aluminum composite vapor chambers, Int. Commun. Heat Mass Transf. 126 (2021) 105449.
[9] G. Patankar, J.A. Weibel, S.V. Garimella, Working-fluid selection for minimized thermal resistance in ultra-thin vapor chambers, Int. J. Heat Mass Transf. 106 (2017) 648–654.
[10] X. Dai, F. Yang, R. Yang, Y.-C. Lee, C. Li, Micromembrane-enhanced capillary evaporation, Int. J. Heat Mass Transf. 64 (2013) 1101–1108.
[11] G. Huang, W. Liu, Y. Luo, T. Deng, Y. Li, H. Chen, Research and optimization design of limited internal cavity of ultra-thin vapor chamber, Int. J. Heat Mass Transf. 148 (2020) 119101.
[12] M. Egbo, A review of the thermal performance of vapor chambers and heat sinks: critical heat flux, thermal resistances, and surface temperatures, Int. J. Heat Mass Transf. 183 (2022) 122108.
[13] Q. Peng, X. Yan, J. Li, L. Li, H. Cha, Y. Ding, C. Dang, L. Jia, N. Miljkovic, Breaking droplet jumping energy conversion limits with Superhydrophobic microgrooves, Langmuir 36 (2020) 9510–9522.
[14] A. Aili, H. Li, M.H. Alhosani, T. Zhang, Unidirectional fast growth and forced jumping of stretched droplets on nanostructured microporous surfaces, ACS Appl. Mater. Interfaces 8 (2016) 21776–21786.
[15] X. Yan, Y. Qin, F. Chen, G. Zhao, S. Sett, M.J. Hoque, K.F. Rabbi, X. Zhang, Z. Wang, L. Li, F. Chen, J. Feng, N. Miljkovic, Laplace pressure driven single-droplet jumping on structured surfaces, ACS Nano 14 (2020) 12796–12809.
[16] Z. Yuan, Z. Hu, F. Chu, X. Wu, Enhanced and guided self-propelled jumping on the superhydrophobic surfaces with macrotexture, Appl. Phys. Lett. 115 (2019).
[17] X. Wang, B. Xu, Z. Chen, Y. Yang, Q. Cao, Lattice Boltzmann simulation of dropwise condensation on the microstructured surfaces with different wettability and morphologies, Int. J. Therm. Sci. 160 (2021) 106643.
[18] P. Zhou, W. Liu, Z. Liu, Lattice Boltzmann simulation of nucleate boiling in micro-pillar structured surface, Int. J. Heat Mass Transf. 131 (2019) 1–10.
[19] S.J. Yue, Z.G. Xu, Numerical simulation on pore-scale pool boiling mechanisms of horizontal gradient porous metals, Int. Commun. Heat Mass Transf. 142 (2023) 106640.
[20] Q. Li, D.H. Du, L.L. Fei, K.H. Luo, Three-dimensional non-orthogonal MRT pseudopotential lattice Boltzmann model for multiphase flows, Comput. Fluids 186 (2019) 128–140.
[21] A. Jaramillo, V. Pessoa Mapelli, L. Cabezas-Gómez, Pseudopotential lattice Boltzmann method for boiling heat transfer: a mesh refinement procedure, Appl. Therm. Eng. 213 (2022) 118705.
[22] X. Li, W. Chan, S. Liang, F. Chang, Y. Feng, H. Li, Numerical investigation on pool boiling heat transfer with trapezoidal/inverted trapezoidal micro-pillars using LBM, Int. J. Therm. Sci. 198 (2024) 108869.
[23] J. Cai, J. Chen, W. Deng, F. Xia, J. Zhao, Towards efficient and sustaining condensation via hierarchical meshed surfaces: a 3D LBM study, Int. Commun. Heat Mass Transf. 132 (2022) 105919.
[24] S. Wu, H. Dai, H. Wang, C. Shen, X. Liu, Role of condensation on boiling heat transfer in a confined chamber, Appl. Therm. Eng. 185 (2021) 116309.
[25] R. Ji, S. Qin, Y. Liu, L. Jin, C. Yang, X. Meng, Analysis of wettability effects on thermal performance of vapor chamber with a hybrid lattice Boltzmann method, Int. J. Heat Mass Transf. 225 (2024) 125315.
[26] H.J. Cho, E.N. Wang, Bubble nucleation, growth, and departure: a new, dynamic understanding, Int. J. Heat Mass Transf. 145 (2019) 118803.
[27] J. Zhou, L. Liu, X. Yang, Y. Zhang, J. Wei, Visualization research on influencing factors of flat heat pipes, Appl. Therm. Eng. 207 (2022) 118193.
[28] M. Wang, J. Wang, N. Pan, S. Chen, Mesoscopic predictions of the effective thermal conductivity for microscale random porous media, Phys. Rev. E 75 (2007) 036702.
[29] J. Li, F. Hong, R. Xie, P. Cheng, Pore scale simulation of evaporation in a porous wick of a loop heat pipe flat evaporator using lattice Boltzmann method, Int. Commun. Heat Mass Transf. 102 (2019) 22–33.
[30] Q. Li, Y. Yu, K.H. Luo, Improved three-dimensional thermal multiphase lattice Boltzmann model for liquid-vapor phase change, Phys. Rev. E 105 (2022) 025308.
[31] S. Gong, P. Cheng, Numerical investigation of droplet motion and coalescence by an improved lattice Boltzmann model for phase transitions and multiphase flows, Comput. Fluids 53 (2012) 93–104.
[32] S. Gong, P. Cheng, Direct numerical simulations of pool boiling curves including heater's thermal responses and the effect of vapor phase's thermal conductivity, Int. Commun. Heat Mass Transf. 87 (2017) 61–71.
[33] C. Zhang, P. Cheng, Mesoscale simulations of boiling curves and boiling hysteresis under constant wall temperature and constant heat flux conditions, Int. J. Heat Mass Transf. 110 (2017) 319–329.
[34] G. Hazi, A. Markus, On the bubble departure diameter and release frequency based on numerical simulation results, Int. J. Heat Mass Transf. 52 (2009) 1472–1480.
[35] I.O. Ucar, H.Y. Erbil, Dropwise condensation rate of water breath figures on polymer surfaces having similar surface free energies, Appl. Surf. Sci. 259 (2012) 515–523.
[36] J. Li, W. Zheng, Y. Su, F. Hong, Pore scale study on capillary pumping process in three-dimensional heterogeneous porous wicks using lattice Boltzmann method, Int. J. Therm. Sci. 171 (2022) 107236.
[37] C. Zhang, P. Cheng, F. Hong, Mesoscale simulation of heater size and subcooling effects on pool boiling under controlled wall heat flux conditions, Int. J. Heat Mass Transf. 101 (2016) 1331–1342.

[38] Y. Zhu, S. Gao, Z. Liu, W. Liu, 3D lattice Boltzmann simulation of self-propelled single-droplet jumping on microstructured surfaces during condensation, Surf. Interfaces 46 (2024) 104055.
[39] S.-C. Wang, Z.-X. Tong, Y.-L. He, X. Liu, Unit conversion in pseudopotential lattice Boltzmann method for liquid–vapor phase change simulations, Phys. Fluids 34 (2022).
[40] X. Liu, P. Cheng, Lattice Boltzmann simulation of steady laminar film condensation on a vertical hydrophilic subcooled flat plate, Int. J. Heat Mass Transf. 62 (2013) 507–514.
[41] T. Wu, T. Wang, Z. Ma, Z. Zhang, W. Liu, Z. Liu, Experimental investigation on the start-up performance of a loop heat pipe with three flat disk evaporators combined, Appl. Therm. Eng. 216 (2022) 119128.